Supplemental for "High resolution three dimensional structural microscopy by single angle Bragg ptychography"

S. O. Hruszkewycz,[1] M. Allain,[2] M. V. Holt,[3] C. E. Murray,[4] J. R. Holt,[5] P. H. Fuoss,[1] and V. Chamard[2]

[1]*Materials Science Division, Argonne National Laboratory, Argonne, Illinois 60439, USA*
[2]*Aix-Marseille University, CNRS, Centrale Marseille, Institut Fresnel, UMR 7249, 13013 Marseille, France*
[3]*Center for Nanoscale Materials, Argonne National Laboratory, Argonne, Illinois 60439, USA*
[4]*IBM T.J. Watson Research Center, Yorktown Heights, New York 10598, USA*
[5]*IBM Semiconductor Research and Development Center, Hopewell Junction, New York 12533, USA*

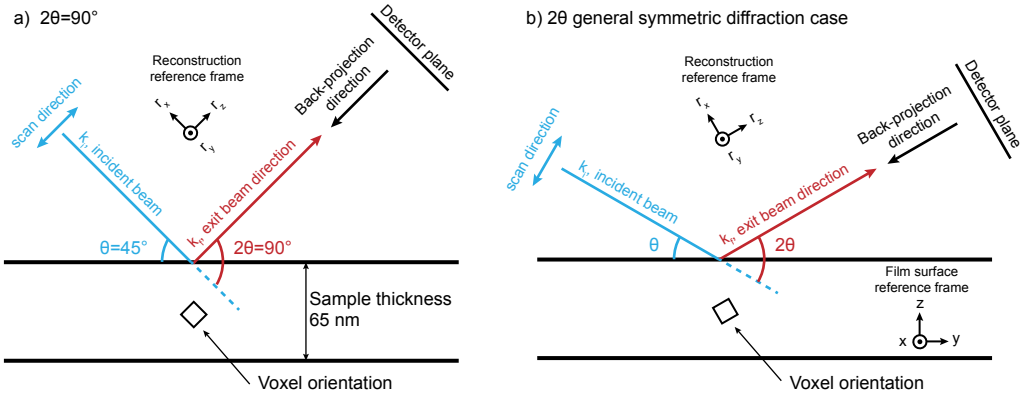

FIG. 1. Suppl. (S1). **Encoding 3D data with 2D diffraction patterns** a) The case of Bragg diffraction from a crystal with a 90° 2θ angle is shown. This geometry is the basis of the analytical derivations presented below because the motion of the beam and the plane of the detector can be simply expressed in one coordinate system. As shown, the area detector plane contains the r_x, r_y directions and displacement of the incident beam is along r_z. The more general symmetric scattering case with a Bragg angle $0^\circ < 2\theta < 90^\circ$ is shown in (b). The arguments made based on the geometry in (a) apply as well to (b) so long as the beam displacement has a significant component of motion along r_z. Note also that the reconstruction reference frame changes as a function of 2θ, thus changing the orientation of an image voxel relative to the film surface reference frame.

Derivation of 3D structural encoding in 3DBPP

In this section, we introduce two analytical derivations to quantify the 3D structural information that is encoded in a set of coherent x-ray diffraction patterns measured from a sample at a single Bragg diffraction angle as a function of variable probe position. We approach this first by assuming that the sample and probe are separable in the (r_x, r_z) coordinate system. Though the simplified derivation assumes separability, this is done solely to simplify the derivation and does not represent a limitation of our technique. This assumption leads to an expression that succinctly underscores the nature of the 3D information contained in a 3DBPP data set. Next, we address the more general case in which the probe and sample cannot be described as separable, leading to a more complete description of the embedded 3D information.

Simplified derivation, assuming separability

We consider the bidimensional case of Bragg scattering with $2\theta = 90^\circ$ depicted in Figure S1(a) (neglecting for now the r_y dimension). The orthonormal reference frame in real space $(\boldsymbol{e}_x, \boldsymbol{e}_z)$ is chosen so that it is the conjugate of the $(\boldsymbol{k}_x, \boldsymbol{k}_z)$ reciprocal space reference frame, and so that $\boldsymbol{k}_x$ is aligned with the detector. By definition, any $\boldsymbol{r}$ (in real space) and $\boldsymbol{q}$ (in reciprocal space) reads

$$\boldsymbol{r} = r_x \boldsymbol{e}_x + r_z \boldsymbol{e}_z \quad \text{and} \quad \boldsymbol{q} = q_x \boldsymbol{k}_x + q_z \boldsymbol{k}_z,$$

with $||\boldsymbol{e}_{x,z}|| = ||\boldsymbol{k}_{x,z}|| = 1$.

As introduced in the main text, the scattering density of the diffracting crystal and the probe function are denoted, respectively, as $\rho(\boldsymbol{r})$ and $P(\boldsymbol{r})$. Let us consider the displacement of the probe along the direction $\boldsymbol{e}_z$ in discrete steps:

$$P_j(\boldsymbol{r}) := P(\boldsymbol{r} - j\Delta \boldsymbol{e}_z), \quad \text{where} \quad j = 0, \cdots M-1.$$

Here, the beam step size is defined as $\Delta \in \mathbb{R}$. In the general case (Figure S1(b)), the displacement of the probe will also have a component along $\boldsymbol{e}_x$, but we neglect this component here because it does not contribute to the encoding of information along $\boldsymbol{e}_z$.

In the far-field regime, the components of the Bragg diffracted field exhibit a 3D dependence that is related to the illuminated scattering volume by a Fourier transform. An x-ray area detector accesses a two-dimensional "slice" through the intensity of this 3D reciprocal space distribution [1, Sec. 6.3.3], depending on the Bragg angle of the sample. The slice, defined by the plane of the detector, corresponds to the squared magnitude of the Fourier transform of a set of line integrals through the scattering volume along the direction of the exit beam wave vector. In other words, the slice at the Bragg condition is the Fourier transform of a 2D projection of the illuminated sample volume [2]. This property of x-ray diffraction is known as the "slice-projection theorem"

(SPT) [1, Sec. 6.3.3], and it has been exploited in modern x-ray computed tomography (CT) reconstruction algorithms. As part of 3D CT imaging, [12, Sec. 6.2], real-space projections at a series of angles are propagated along the direction of integration, a process known as backprojection [3]. Backprojection represents a 2D projection in three dimensions in a manner consistent with the SPT, and this concept was integrated as part of our approach.

As a result of the Slice Projection Theorem [4, Sec 6.3.3], when a Bragg condition is satisfied, the coherent far-field intensity pattern observed in the detector is given by:

$$I(q_x) = |\tilde{\psi}_j(q_x, q_z = 0)|^2 \tag{1}$$

where $\tilde{\psi}_j$ is the Fourier transform [4] (indicated by the " $\tilde{}$ " symbol) of the j-th sample exit-field:

$$\psi_j(\boldsymbol{r}) := P(\boldsymbol{r} - j\Delta \boldsymbol{e}_z)\rho(\boldsymbol{r}). \tag{2}$$

As noted in the main text, we adopt the convention that in a coherent Bragg diffraction imaging experiment, the origin of reciprocal space $(q_x = 0, q_y = 0, q_z = 0)$ corresponds to a reciprocal space Bragg peak denoted by the reciprocal space vector $\mathbf{G_{HKL}}$ for a given HKL Bragg reflection [5]. For the purposes of this derivation, we assume that the phases of $\tilde{\psi}_j$ are known (*i.e.* an appropriate phase retrieval strategy was implemented, such as the one we presented in the main text). Thus, we define the following quantity:

$$\Psi_j(q_x) := \tilde{\psi}_j(q_x, q_z = 0). \tag{3}$$

$\{\Psi_j(q_x)\}_{j=0}^{J-1}$ represents a set of complex-valued far-field wave fields at J different probe positions observed at a fixed sample angle (no rocking curve). The question we seek to answer is whether structural information about the sample along $\boldsymbol{e}_z$ is encoded in the measurements $\{\Psi_j(q_x)\}_{j=0}^{J-1}$. To answer this question, we begin by expressing Equation (2) as:

$$\psi_j(\boldsymbol{r}) = \rho(\boldsymbol{r}) \times \left[P(\boldsymbol{r}) \otimes \delta(\boldsymbol{r} - j\Delta \boldsymbol{e}_z)\right],$$

where $\otimes$ is the convolution operator. Taking the Fourier transform leads to:

$$\tilde{\psi}_j(\boldsymbol{q}) = \tilde{\rho}(\boldsymbol{q}) \otimes \left[\tilde{P}(\boldsymbol{q}) \times e^{-iq_z(j\Delta)}\right] \times \frac{1}{(2\pi)^2} \tag{4}$$

$$= e^{-iq_z(j\Delta)} \int_{\boldsymbol{q}'} \tilde{\rho}(\boldsymbol{q}')\tilde{P}(\boldsymbol{q} - \boldsymbol{q}')e^{iq'_z(j\Delta)}\, \mathrm{d}\boldsymbol{q}' \times \frac{1}{(2\pi)^2} \tag{5}$$

We now assume that ρ and P are both *separable* functions

$$\rho(\boldsymbol{r}) = \rho_z(r_z) \times \rho_x(r_x)$$
$$P(\boldsymbol{r}) = P_z(r_z) \times P_x(r_x)$$

which, in turns, implies that their Fourier transform are also separable functions

$$\tilde{\rho}(\boldsymbol{q}) = \tilde{\rho}_z(q_z) \times \tilde{\rho}_x(q_x)$$
$$\tilde{P}(\boldsymbol{q}) = \tilde{P}_z(q_z) \times \tilde{P}_x(q_x)$$

This assumption allows us to most clearly demonstrate how spatial information along $\boldsymbol{e}_z$ can be encoded without performing a rocking curve. Towards this aim, we express Equation (5) as:

$$\tilde{\psi}_j(\boldsymbol{q}) = \left(\tilde{\rho}_x \otimes \tilde{P}_x\right)(q_x) \times \left[\int_{q'_z} \tilde{\rho}_z(q'_z)\tilde{P}_z(q_z - q'_z)e^{iq'_z(j\Delta)}\, \mathrm{d}q'_z\right] e^{-iq_z(j\Delta)} \times \frac{1}{(2\pi)^2} \tag{6}$$

According to Equation (3), at a single Bragg angle we can only access the far-field diffracted wave field at $q_z = 0$. The reciprocal space information we collect as a function of probe position can therefore be expressed as:

$$\Psi_j(q_x) = \left(\tilde{\rho}_x \otimes \tilde{P}_x\right)(q_x) \times g_z(r_z = j\Delta) \times \frac{1}{(2\pi)^2} \tag{7}$$

were g_z is the inverse Fourier transform of $\tilde{g}_z(q) = \tilde{\rho}_z(q) \times \tilde{P}_z(-q)$. Another convenient expression for Equation (7) is:

$$\Psi_j(q_x) = \left(\tilde{\rho}_x \otimes \tilde{P}_x\right)(q_x) \times (\rho_z \otimes P'_z)(r_z = j\Delta) \times \frac{1}{(2\pi)^2} \tag{8}$$

where $P'_z(r_z) := P_z(-r_z)$. Finally, we can derive the dependence in real space by taking the inverse Fourier transform along q_x, denoted as $\mathcal{F}^{-1}_{q_x}$. We define:

$$\begin{aligned} g(r_x, r_z = j\Delta) &:= \left(\mathcal{F}^{-1}_{q_x}\Psi_j\right)(r_x) \\ &= P_x(r_x)\,\rho_x(r_x) \times (\rho_z \otimes P'_z)(r_z = j\Delta) \times \tfrac{1}{(2\pi)} \end{aligned}$$

This expression shows that a set of fields observed at a fixed detector plane does encode information about the sample in the direction normal to the detector plane. This information is contained in the convolution term which is a function of r_z, dependent on the scanning of the probe in that direction. Hence, in the Bragg geometry, some structural information contained along r_z that would be recorded with a rocking curve in a typical CXDI experiment is encoded in a set of single-angle diffraction patterns when measured with a scanned finite-sized focused beam. This conclusion also holds true when a third dimension (perpendicular to the page) is added. This is due to the fact that structural information about the sample along r_y is directly encoded in reciprocal space with an area detector that can access q_x and q_y, and does not change the discussion about sample structure along r_z. Similarly, these conclusions hold when removing the assumption of separability as shown below.

General derivation, for arbitrary samples and probes

For sake of completeness, we provide an analytical derivation for the case when ρ and P are *not* separable along r_x and r_z, as is typically the case. We start again from the FT of (2), considering the Bragg $2\theta = 90^\circ$ geometry:

$$\tilde{\psi}_j(\boldsymbol{q}) = \int_{r_x}\left[\int_{r_z}\rho(r_x, r_z)P(r_x, r_z - j\Delta)e^{-ir_z q_z}\mathrm{d}r_z\right]e^{-ir_x q_x}\mathrm{d}r_x \tag{9}$$

Because the term in brackets is a one-dimensional FT along r_z, we can express

$$\tilde{\psi}_j(\boldsymbol{q}) = \int_{r_x}\tilde{\rho}_{q_z}(r_x, q_z) \otimes_{q_z}\left[\tilde{P}_{q_z}(r_x, q_z)e^{-iq_z(j\Delta)}\right]e^{-ir_x q_x}\mathrm{d}r_x \times \frac{1}{(2\pi)} \tag{10}$$

where $\tilde{f}_{q_z}(r_x, q_z)$ denotes the one-dimensional FT along r_z of a given real-space function $f(r_x, r_z)$, and $\otimes_{q_z}$ is the one-dimensional convolution operator along q_z. To calculate this quantity solely in the plane of the detector oriented at a Bragg condition, we set $q_z = 0$ and rewrite the convolution. This leads to

$$\Psi_j(q_x) = \int_{r_x}\left[\int_{q'_z}\tilde{\rho}_{q_z}(r_x, q'_z)\tilde{P}_{q_z}(r_x, -q'_z)e^{iq'_z(j\Delta)}\mathrm{d}q'_z\right]e^{-ir_x q_x}\mathrm{d}r_x \times \frac{1}{(2\pi)}$$

that we finally express as

$$\Psi_j(q_x) = \int_{r_x} g(r_x, r_z = j\Delta)e^{-ir_x q_x}\mathrm{d}r_x \times \frac{1}{(2\pi)} \tag{11}$$

with

$$g(r_x, r_z) := (\rho \otimes_{r_z} P')(r_x, r_z) \tag{12}$$

where $P'(r_x, r_z) := P(r_x, -r_z)$. So, as in the simpler separable case, the field in the plane of the detector does in fact encode spatial information along $\boldsymbol{e}_z$ when measured as a function of beam displacement in that direction, while the information along $\boldsymbol{e}_x$ is directly extracted in the reciprocal space direction q_x.

In summary, the spatial diversity "embedded" within the ptychographic experiment produces a *spatial sampling* that extracts the structural information about ρ along $\boldsymbol{e}_z$. We have demonstrated analytically the sensitivity of 3DBPP to sample structure

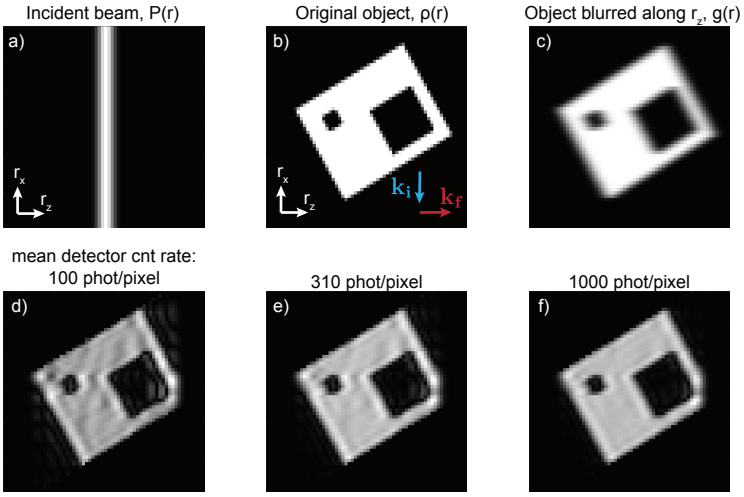

FIG. 2. Suppl. (S2). **3DBPP with varying signal-to-noise ratios** A numerical study was done to determine the extent to which SNR impacts the resolution of 3DBPP reconstructions along the backprojection direction r_z. Panels (a) shows the gaussian probe used, (b) the object ρ, and (c) the convolution of the two $g(r)$. Numerical diffraction patterns were generated at different probe positions, differing levels of noise was introduced to these intensity patterns, and 3DBPP phase retrieval was performed. Panels (d-f) show the resulting image reconstructions at different signal-to-noise ratios (SNR). As SNR improves, the high frequency components that are highly damped are recovered to some degree, resulting in varying degrees of deconvolution of the probe from the object with 3DBPP.

along the exit beam direction – a result that is made possible by the properties of a high-angle Bragg peak measured with a scanning probe. Finally, we note that the analytical analysis above does not provide a reconstruction strategy to retrieve the sample ρ from the experimental dataset. More specifically, because only diffracted intensities are measured, g cannot be accessed directly and the practical reconstruction of ρ requires an iterative phase retrieval algorithm (as outlined in the Methods section of the main letter, our 3DBPP reconstructions were performed with a OS/PIE iteration). Moreover, such an iterative reconstruction strategy provides an *implicit* deconvolution of the probe along $\boldsymbol{e}_z$, hence bringing some sub-beam-size resolution capabilities along that direction. This later capability is further investigated in the following section.

Probe deconvolution in the backprojection direction with 3DBPP

From Equation 11 and 12 above, we conclude that the diffracted fields are related to the function g which contains all the spatial information that may be retrieved from the sample. Examining this further, we take the FT of 12 and get $\widetilde{g} = \widetilde{\rho}\,(q_x, q_z) \times \widetilde{P}(q_z)$. This relation indicates that the spectrum of the probe along r_z impacts the resolution limit in 3DBPP. If some components of $\widetilde{P}(q_z)$ are vanishingly small, the corresponding component in $\widetilde{\rho}$ is lost and cannot be retrieved. However, components of $\widetilde{\rho}$ corresponding to small but non-zero values of $\widetilde{P}(q_z)$ (*e.g.* near the tails of the probe spectrum) *may* or *may not* be recovered depending on the signal-to-noise ratio (SNR) available. With moderate or low SNR, we do not expect that frequency components can be retrieved beyond the the limit of the probe bandwidth envelope, hence giving a final reconstruction that is mostly equivalent to g. However, as the SNR increases, damped frequency components can be reliably retrieved, providing some degree of sub-beam resolutions along r_z. In this case, high frequency terms in the object spectrum damped by the probe spectrum are amplified, resulting in a Fourier deconvolution performed implicitly via 3DBPP phase retrieval.

Figure S2 demonstrates the link between SNR in the measured data and the potential to reconstruct images at resolutions higher than the point spread function (PSF) of the incident beam in the direction of back-propagation. A numerical study was performed using a purely real gaussian beam with a FWHM along r_z of 4.1 pixels (a), and a simulated 3D crystalline object $\rho(\boldsymbol{r})$ (b) similar to the one featured in the main text. The incident beam direction $\mathbf{k_i}$ is perpendicular to r_z, and the exit beam direction $\mathbf{k_f}$ is parallel to r_z, such that the Bragg 2θ angle is 90°. A rendering of g (probe-limited resolution along the r_z direction) is shown in (c). The blurring of g along r_z comes about because the spectrum of the object ρ is damped by the envelope of the probe spectrum along r_z, especially at higher spatial frequencies. However, because the envelope function of the probe spectrum is non-zero and damps (rather than truncates) high spatial frequencies in $\widetilde{\rho}$, the 3DBPP inversion algorithm can inherently deconvolve the probe from the object with sufficient SNR in the measured data.

To demonstrate this, a numerical ptychographic experiment was simulated: coherent Bragg diffraction patterns were generated at every position (*via* Equations 1 and 2 in the main text) of a 41×11 point raster scan of the beam (along the r_z, r_y

directions) with a $\Delta = 1$ pixel step size. By introducing Poisson noise, data sets with various SNR were generated, and 3DBPP reconstructions were performed as described in the main text. Figure S2 shows cuts through the resulting 3DBPP reconstructions (d-f) under these different noise conditions. By comparing these reconstructions with the original and blurred objects (b,c), we see that with lower SNR, the resolution of the reconstruction along r_z is limited by the PSF of the beam. As SNR increases, high frequency components that would be highly damped by the probe spectrum are partially recovered. Thus, partial deconvolution of the beam PSF along r_z is inherently achievable with the 3DBPP iteration, though the extent to which this is realized depends on the SNR in the measured diffraction patterns. We emphasize that in the experimental demonstration presented in the main text, the SNR of our data is such that only modest gains in r_z resolution beyond the PSF of the beam were achieved. We expect this situation to be commonly encountered under realistic experimental conditions.

Comparison of Bragg and transmission geometries

In order to emphasize the role of the Bragg geometry in 3DBPP, we present a comparison between images reconstructed from diffraction patterns simulated in both the Bragg and forward scattering geometries (Figure S3). Here, we assume that the forward scattering geometry entails a small-angle measurement in which structural information is collected over angles $< 2^\circ$ from the direct beam. In both cases, intensity patterns give access to a 2D projection of the illuminated volume. However, the relationship between the exit beam vector $\mathbf{k_f}$ (the projection direction) and the incident beam direction $\mathbf{k_i}$ in the two cases leads to very different three dimensional information content.

As outlined in the main text, in the Bragg geometry $\mathbf{k_i}$ and $\mathbf{k_f}$ are not colinear. Thus, scanning the localized incident beam in the plane normal to its propagation direction with overlapping steps enables the 3D structure of the sample to be reconstructed using 3DBPP. In this numerical example, the phases of the far field intensity patterns at each position are known *a priori*. Therefore, a summation of the backprojections at each scan point multiplied by each respective probe can be done: $\sum_j P_j^* \mathcal{R}^\dagger \mathcal{F}^{-1} \Psi_j$. This summation of localized backprojections is shown in Figure S3(b) for the numerical sample described in Figure 2 of the main text. The resulting image shows that the three dimensional sample structure can be resolved from a set of 2D projections provided that $\mathbf{k_i}$ and $\mathbf{k_f}$ are separated by a non-zero angle typical of hard x-ray Bragg diffraction. This process yields an image that is a blurred version of the original object, and demonstrates the basic mechanism by which 3D structural sample information is encoded in a high-angle Bragg ptychography data set without requiring angular diversity. Starting with the same numerical diffraction information in the form of intensity patterns, 3DBPP was used to recover the phases and reconstruct the object. As shown in Figure S3(c), the 3DBPP reconstruction is sharper than the summation of localized back projections, and a sub-beam-size resolution is achieved (see next section) as has been shown in transmission-geometry ptychography experiments [6].

As compared with the Bragg geometry, $\mathbf{k_i}$ and $\mathbf{k_f}$ are mostly colinear in a scanning beam transmission geometry diffraction experiment (the maximum angle between $\mathbf{k_i}$ and $\mathbf{k_f}$ is typically $< 2^\circ$ and the central ray path corresponds to $2\theta = 0^\circ$), as shown in Figure S3(d). As a result, no structural information along the propagation direction of the incident beam is encoded in a 2D diffraction pattern measured in this geometry. This is demonstrated by the fact that both the summation of localized backprojections and the 3DBPP reconstruction of the numerical test object yield images that show the projected density profile of the object stretched along the $\mathbf{k_f}$ direction and resolve no structure along the exit beam. In other words, only the backprojection of the original object within the scanned field of view was reconstructed. In order to recover the three dimensional structure of the sample from such a scattering geometry ($2\theta \sim 0^\circ$), scans must be done as a function of sample orientation and computed tomography algorithms must be used for 3D imaging [7].

Three-dimensional dependence of resolution

As in other coherent diffraction imaging techniques, the resolution of a 3DBPP reconstruction varies along different directions. In the plane perpendicular to $\mathbf{k_f}$, the resolution is primarily determined by the extent of the diffraction envelope measured about the Bragg peak, which sets the effective numerical aperture in that plane. This type of q-range resolution limitation is typical of diffractive imaging microscopy techniques, and accurately describes the experimental resolution of the SiGe reconstruction along the axes of the detector plane.

However, the factors that limit image resolution in the projection direction are less obvious. The resolution in the $\mathbf{k_f}$ direction does not stem simply from reciprocal space sampling, but is influenced by the scanning probe nature of the diffraction experiment. In order to investigate the dependence of resolution along $\mathbf{k_f}$ as a function of scattering angle, beam size, and beam step size; 3DBPP reconstructions were done using calculated noise-free data from the numerical object shown in Figure S3. Various symmetric Bragg peaks were simulated with $2\theta = \angle \mathbf{k_i k_f} = 50, 60, 70, 90^\circ$, and an exact support was used that conformed to the outer edges of the sample, leaving the voids to be reconstructed by the algorithm. Real gaussian beams with a FWHM of 4

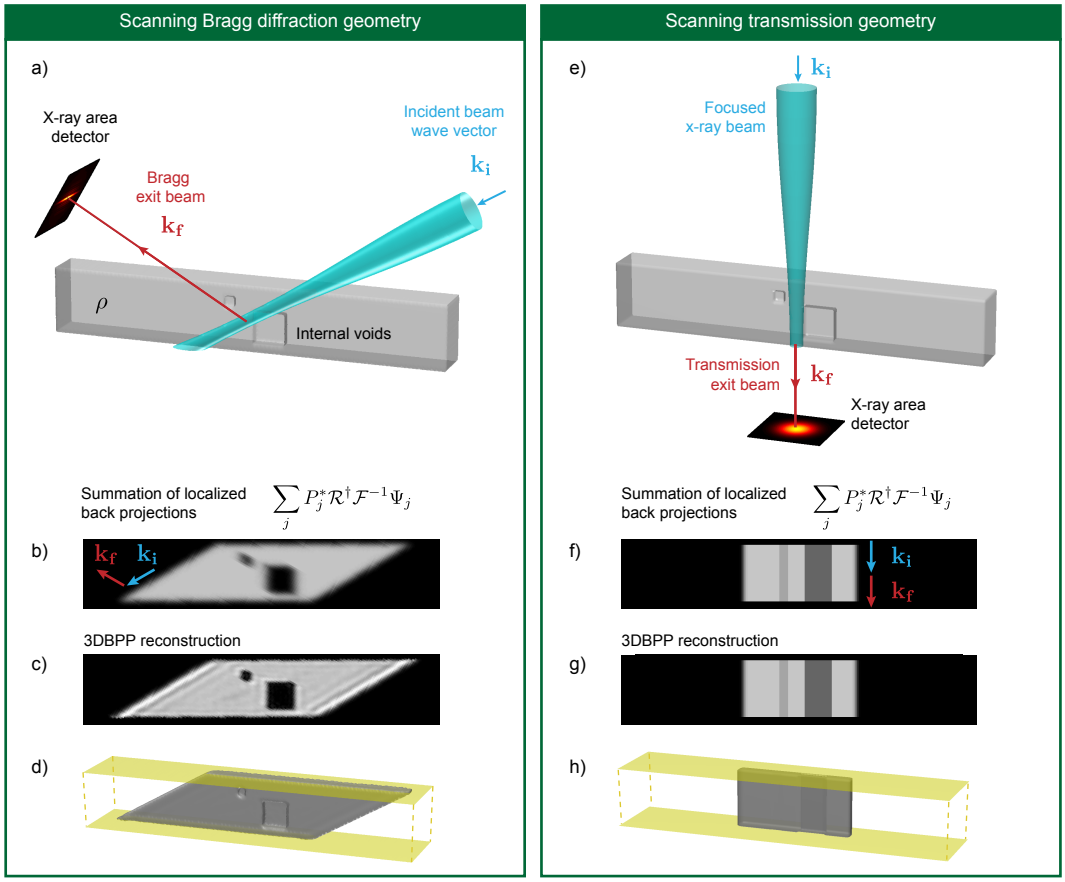

FIG. 3. Suppl. (S3). **Bragg vs. transmission geometry 3DBPP** (a) The Bragg geometry is simulated for 3DBPP of the test object featured in Figure 1 in the main text. (b) Because the phases of each diffraction pattern are known in this simulation the quantity $\sum_j P_j^* \mathcal{R}^\dagger \mathcal{F}^{-1} \Psi_j$ can be calculated, referred to as the summation of localized backprojections. (c,d) The result of 3DBPP phase retrieval using simulated noise-free diffraction patterns is shown. e) The same test object is scanned with the same focused beam in a transmission geometry. (f) The summation of localized backprojections does not accurately represent the voids, nor does the 3DBPP reconstruction (g,h) because 3D sample information is not encoded in a transmission ptychography experiment.

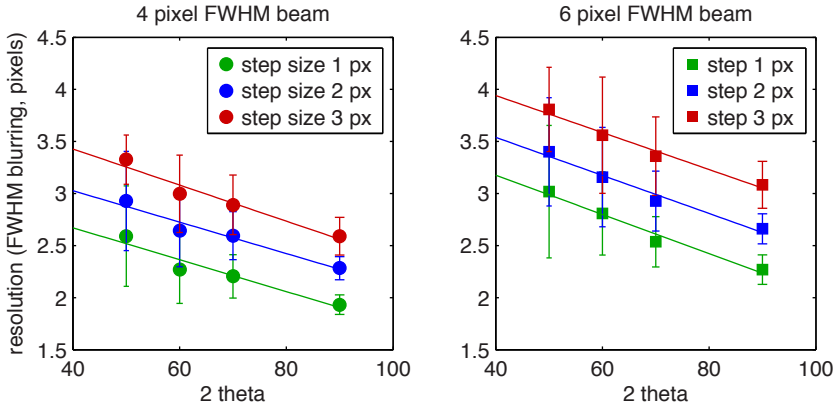

FIG. 4. Suppl. (S4). **Dependence of resolution:** 3DBPP resolution along the $\mathbf{k_f}$ direction is shown as a function of step size, scattering angle, and beam size from reconstructions of the numerical object shown in Figure S3(c) at a series of symmetric Bragg reflections. Noise-free data was used with a tight support that was the exact outer shape of the original object in order to isolate the effects of the other parameters indicated here. The solid lines are linear fits to each data set and serve to highlight the dependence of resolution on Bragg angle, step size, and beam size.

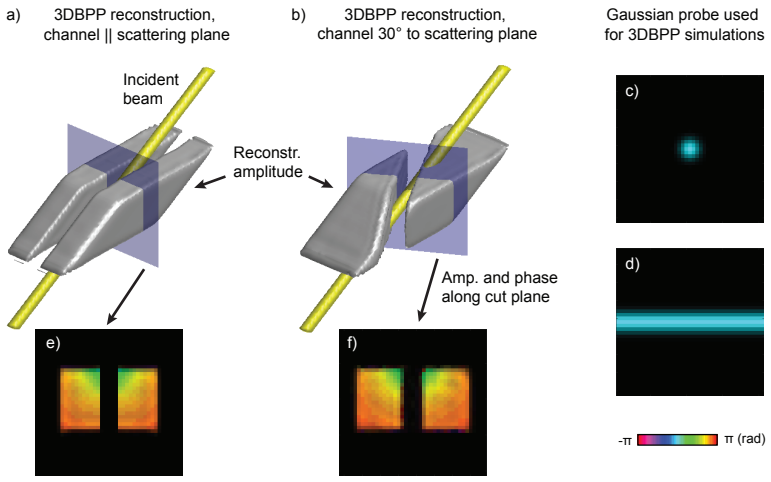

FIG. 5. Suppl. (S5). **Dependence of feature orientation:** A model crystal was created to replicate the structural features of the channelled SiGe sample in the main text. Simulated 3DBPP experiments were performed on the crystal in two different orientations: (a) with the channel walls parallel to the scattering plane (as in the experimental demonstration), and (b) with the channel rotated by 30° from the scattering plane about the film surface normal. Both orientations faithfully reconstruct the features of the channel. The gaussian beam (4.1 pixels FWHM) shown in (c) in cross-section and (d) along its length was used to generate diffraction patterns for this test. The same probe, which does not have any phase diversity, was used to generate diffraction patterns featured in Figure 2 in the main text. (e,f) show that the internal phase of both channel orientation was successfully recovered. (c-f) show amplitude as brightness and phase as color, according to the legend in the lower right.

and 6 pixels were used in this comparison. The resolution in the $\mathbf{k_f}$ direction of the resulting reconstructions are shown in Figure S4. They are expressed as the FWHM of a gaussian blur filter kernel applied to a set of amplitude line profiles along $\mathbf{k_f}$ through the original object fitted to the corresponding amplitude profiles of the reconstruction. The mean value of a set of 15 line profile fits from each reconstruction are plotted with error bars of one standard deviation. Linear fits to the data are shown that are meant to be guides to the eye. As shown in the Figure, sub-beam-size resolution can be achieved along the $\mathbf{k_f}$ direction over an angular range of $2\theta \sim 40 - 90°$ for the conditions surveyed here. The resolution does, however, have a clear dependence on scattering angle, step size, and beam diameter. Though a description of the precise dependence and limits of 3DBPP resolution along $\mathbf{k_f}$ is complex and requires further investigation, based on this numerical study we conclude that the resolution of a 3DBPP imaging experiment is highest when the beam diameter and step size are minimized (though these parameters have limits in practice and are linked, as noted in the first Supplemental section). Furthermore, the resolution has a strong dependence on scattering angle, which we expect to be optimized when $\mathbf{k_f}$ is normal to $\mathbf{k_i}$. As the 2θ angle approaches 0°, we encounter the situation described in Figure S3(e-h), in which all structure along the $\mathbf{k_f}$ direction is lost.

In practice, the dependence and interconnectivity of the 3D resolution function of a 3DBPP reconstruction is undoubtedly a complex function of Bragg angle, beam size, beam amplitude and phase profile, the spatial spectrum of the beam, beam step size, experimental positioning accuracy and drift, signal-to-noise ratio, reconstruction algorithm, and other factors. Furthermore, the experimenter has considerable latitude in defining a support. In our experimental reconstruction, the support was defined by a pair of parallel planes that were consistent with the expected thickness of the diffracting crystal in the out-of-plane direction. In the case of crystals that have thin-film-like geometries, we find that this is a suitable choice of support. In addition, the thickness of such crystals can be readily determined by other methods and can even be estimated from the diffraction patterns in the 3DBPP data set. We note that an effective support for a 3DBPP experiment primarily fulfills the role of a phase reference along $\mathbf{k_f}$, and thus can take on forms other than the ones we employed here.

We also performed simulated 3DBPP reconstructions to determine the sensitivity of our method to the orientation of the SiGe channels relative to the scattering plane in the experimental demonstration in the main text. As shown in Figure S5, two orientations were simulated: (a) with the channel walls parallel to the scattering plane, and (b) with the channel walls rotated 30° away from it, about the surface normal of the film. A 4.1 pixel FWHM gaussian probe with no phase structure (the same as used in Figure 2 of the main text) was used to generate simulated data from both structures (beam profile shown in c,d with brightness as amplitude and color as phase). Identical scans of the beam were performed (21×25 point raster scan with 2 pixel steps), and 3DBPP reconstructions were performed. The 3D reconstructed channel morphologies are shown in (a,b), and both reconstructions yielded the appropriate channel orientation without difficulty. To more closely mimic the SiGe channel mapped experimentally, a phase variation was introduced to the model channels that intensifies at the walls of the channel near the upper surface. Figure S5(e,f) shows that for both orientations, this phase structure was retrieved successfully. Thus, both

the morphology and internal strain of a channel-like structure presented in this work can be reconstructed in 3D for different in-plane channel orientations.

In Figure S10, we explore the dependence of 3D image fidelity as a function of support size by way of numerical simulation of a cubic crystal. Noise-free intensity patterns were generated from a 7×7 grid of beam positions illuminating a simple cube with an edge-length of 10 pixels. The angle between $\mathbf{k_i}$ and $\mathbf{k_f}$ was 60°, as indicated in the Figure. The plot in Figure S10(a) shows the sum squared difference of pixels between the original cube ρ_{orig} and the resulting reconstruction ρ determined according to $||\rho - \rho_{orig}||^2$ as a function of support size. The support used in each case was cubic with edge lengths as shown in the plot. Two hundred 3DBPP OS/PIE iterations were performed to generate a reconstruction, and reconstructions were done five times in each case. The mean $||\rho - \rho_{orig}||^2$ value is plotted with error bars of one standard deviation, and values of $||\rho - \rho_{orig}||^2$ were determined accounting for the differences in origin of ρ relative to that of the ρ_{orig}. As the edge length of the support increases from being exactly the size of ρ_{orig} to being nearly twice its size, $||\rho - \rho_{orig}||^2$ increases and the reconstructions contain more artifacts that clearly affect the resolution. However, this test demonstrates that the cube reconstructions are recognizable even with a support that is nearly eight times the volume of the original object, suggesting that the choice of support is rather flexible in 3DBPP. As a point of comparison, we consider single-particle Bragg coherent diffraction imaging from a rocking curve measurement. Under these conditions, a tight support is critical for successful image reconstruction, to the point that shrink-wrapping is employed [8]. In this work, 3DBPP reasonably reconstructs a cube with a support that is nearly six times larger in volume than the object itself, conditions under which conventional Bragg CDI typically fails altogether [9]. On the other hand, 2D ptychography has been shown to need no support whatsoever. On this spectrum, our new method falls in between the two.

Fourier ring correlation analysis for direction-dependent resolution determination of the experimental reconstruction

To determine the spatial resolution of the experimental SiGe 3DBPP reconstruction presented in the main text, we employed a modified Fourier shell correlation (FSC) method, a technique used to estimate spatial resolution in small-angle ptychography measurements [11] and cryo-TEM 3D imaging experiments [10]. In this section, we expound upon the details of the FSC analysis used in this work which are outlined in the Methods section of the main text.

FSC requires that two independently-reconstructed images of the same area be compared and spectrally correlated. Here, we produce two independent 3DBPP reconstructions by splitting up the data into two "half-sets," as is done in cryo-TEM data. In this work, the half-data sets consist of even- and odd-indexed positions along the scanning spirals. The split positions are shown in Figure S6. 3DBPP reconstructions of each half-data set were performed exactly as the full data were reconstructed in the main text.

These two half-set reconstructions were compared with FSC analysis (shown in Figure S7). The analysis was done by correlating the 3D Fourier spectra of both reconstructions. A correlation coefficient was determined [10, 11] for all pixels in a shell in Fourier space one pixel wide, centered about the origin. Thus, the correlation coefficient can be plotted against spatial frequency, and a correlation threshold cutoff can be applied such that spatial frequencies falling below the cutoff are considered below the resolution of the measurement. Using a 1/2-bit correlation cutoff of 0.207 (as proposed in Refs [10, 11]), we find that the highest meaningful spatial resolution above noise in the reconstructed image is 9.8 nm. This high spatial resolution estimate comes about because the 3DBPP reconstruction is constrained by a 90-nm-thick support that undoubtedly has an influence on the resolution in this direction. To resolve this issue, we utilized a direction-sensitive implementation of FSC.

To estimate spatial resolution as a function of azimuthal angle along different directions, we slightly adapted the FSC method, as described here. Shown in Figure S8(a) is the reconstructed amplitude surface of the SiGe crystal generated from one of the two half-data sets, oriented in the (r_x, r_y, r_z) frame. The green isosurface in (b) shows the corresponding Fourier transform amplitude which was used for FSC analysis in Figure S7. To estimate spatial resolution along specific azimuthal directions, we introduce a cylindrical mask in Fourier space that passes through the origin (purple isosurface in S8(b)). Performing FSC analysis only on the set of Fourier-space voxels contained in the mask provides an estimate of spatial resolution along the principle axis of the cylinder. For example, in Figure S7, all voxels outside the cylinder will be set to zero, and an FSC analysis of this modified spectrum will be done. Because the long axis of the cylinder is oriented along the q_x direction, the resulting FSC resolution estimate will correspond mostly to features in the image along r_x. In this manner, the orientation of the cylindrical mask can be varied so as to estimate spatial resolution along different azimuthal directions.

In our analysis, we varied the orientation of this mask in 10° increments along three equatorial planes (red, blue, and black circles) corresponding to the (r_x, r_z), (r_y, r_z), and (r_x, r_y) planes in the sample. For each mask orientation, FSC plots such as the one in Figure S7 were generated and the 0.207 correlation criterion was applied to obtain a spatial resolution estimate. The results are show in Figure S9.

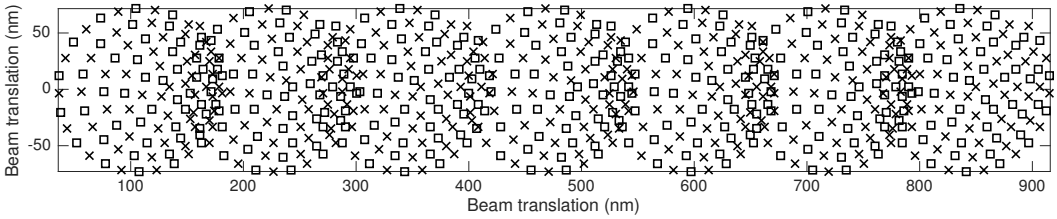

FIG. 6. Suppl. (S6). **Splitting data for FSC** To perform FSC analysis of the SiGe 3DBPP reconstruction in the main text, we split our data set into even and odd-indexed spiral positions (depicted as X's and squares respectively). These two half-data sets were used to generate independent 3DBPP image reconstructions for spectral analysis with FSC.

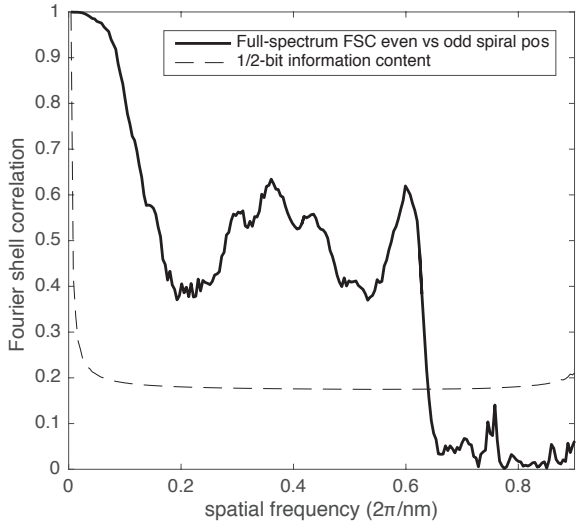

FIG. 7. Suppl. (S7). **FSC analysis** A FSC analysis of two half-data sets is shown. Reconstructions of even-indexed and odd-indexed probe positions were performed under the same conditions as the full data set. Using a 1/2-bit threshold (as suggested in [11]) gives a resolution limit of 9.8 nm.

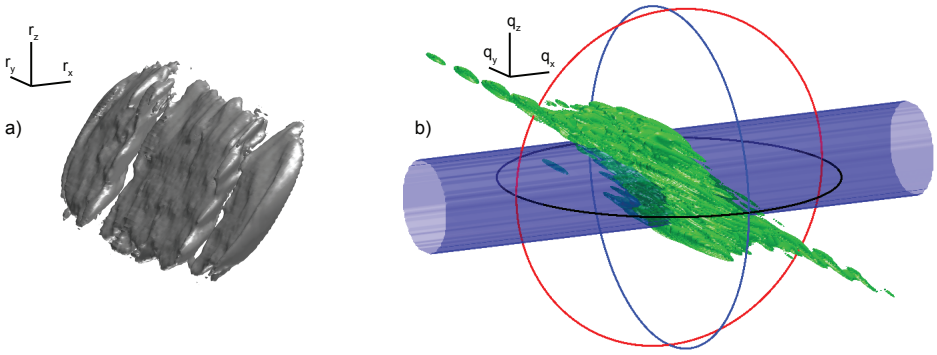

FIG. 8. Suppl. (S8). **Direction-sensitive FSC** The FSC analysis in the previous Figure averages over all directions and yields the highest spatial resolution without regard to orientation. Here, we modify the FSC approach to gain insight as to spatial resolution along different directions. In (a), an isosurface rendering of the 3D density of the even-spiral-index reconstruction is shown in the (r_x, r_y, r_z) reference frame. The (r_x, r_y) directions are parallel to the face of the area detector and $r_z||\mathbf{k_f}$ corresponds to the direction of backprojection. The magnitude of the Fourier transform of this reconstruction is shown in (b) (green isosurface rendering). We modified the FSC analysis to estimate spatial resolution along different directions by introducing a cylindrical mask in the Fourier domain (purple isosurface in (b)). FSC analysis was performed only on Fourier-domain pixels within the cylindrical mask. The calculation was performed as a function of cylinder orientation. The cylinder was rotated about the origin to isolate azimuthal directions in the (r_x, r_y), (r_x, r_z), and (r_y, r_z) planes. (This was done by processing the cylinder in 10° increments along the black, red, and blue equatorial circles.)

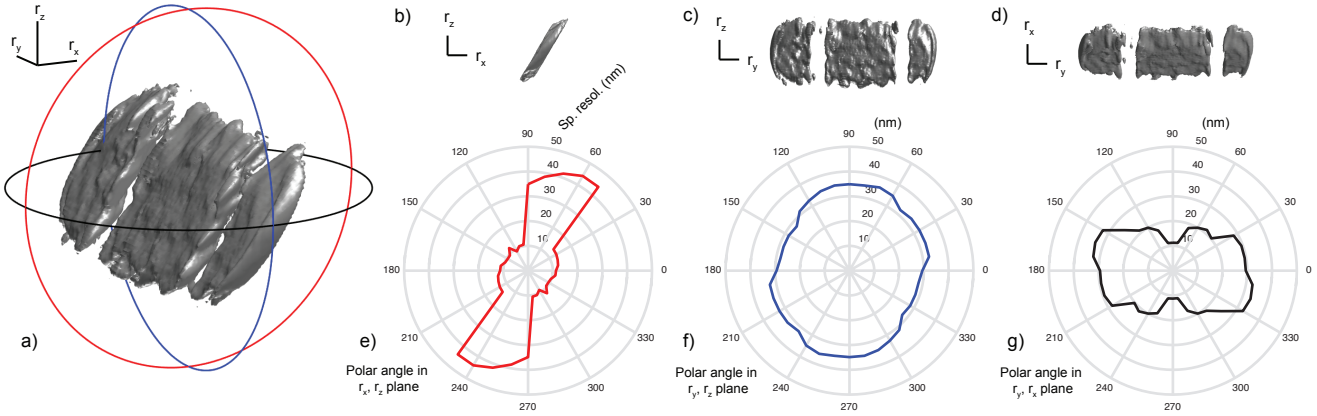

FIG. 9. Suppl. (S9) **Estimating 3DBPP spatial resolution.** Direction-sensitive FSC results are shown. The even-spiral-index reconstruction is shown in (a) along with the equatorial planes in which FSC resolution was determined. The view of the 3D reconstruction in these equitorial planes is shown in (b-d). The spatial resolution as a function of azimuthal direction in these planes determined via the modified FSC approach described above is shown in (e-g). It is clear that the highest spatial resolution is achieved in the direction normal to the SiGe film surface. Along this direction, the reconstruction is constrained by a 90-nm-thick support that undoubtedly has an influence on the resolution in this direction. In all other directions, the spatial resolution is in the range of 20-35 nm.

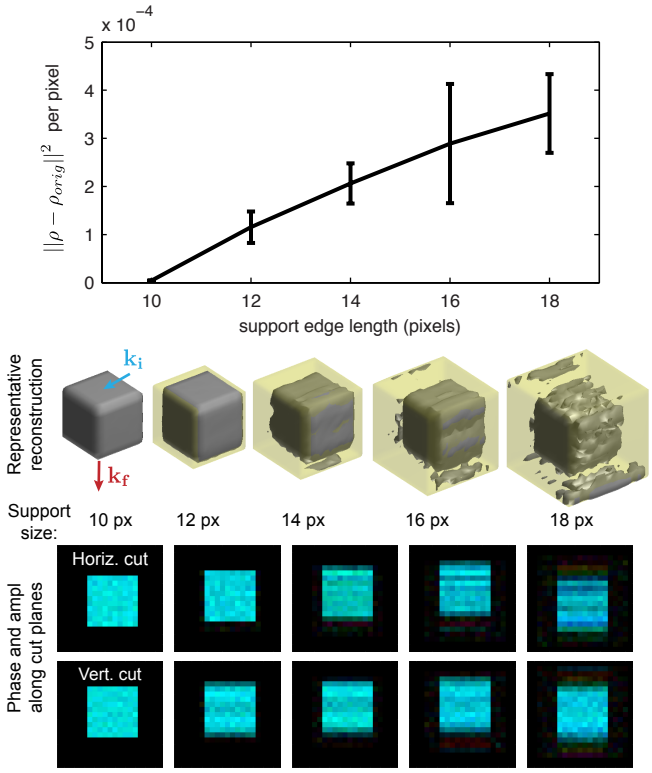

FIG. 10. Suppl. (S10). **Effect of support in 3DBPP.** 3DBPP reconstructions of a cubic numerical test object were done using different sized cubic supports. At each support condition, five separate reconstructions were conducted. The mean final real-space object error $||\rho - \rho_{orig}||^2$ is shown as a function of support size in (a). (b) Examples of a reconstruction from each condition are shown (gray isosurface) along with the corresponding support (yellow surface). The geometry of the experiment is conveyed by the incident and exit $\mathbf{k_i}$ and $\mathbf{k_f}$ vectors. The lowest two rows show the amplitude and phase along two cut planes through the 3DBPP reconstructions shown above. Amplitude is shown as brightness and phase as color.

Phase retrieval pseudocode for 3DBPP

// Given quantities
$\{I_j\}_{J=0}^{J-1}$ (intensity patterns), $\{P_j\}_{J=0}^{J-1}$ (probes), $\rho^{(0)}$ (starting estimate);

for $k = 0 \cdots$ **do** // The main loop...

// Prepare the current estimate...
$\rho^{(k,0)} \longleftarrow \rho^{(k)}$

for $j = 0 \cdots J-1$ **do** // Loop over the probe positions...

// Proposed far-field...
$\Psi^{(k;j)} \longleftarrow \mathcal{F}\mathcal{R}P_j\rho^{(k;j)}$

// Gradient for the current position...
$\partial_j \longleftarrow P_j^*\mathcal{R}^\dagger\mathcal{F}^{-1}\left(\Psi^{(k;j)} - \sqrt{I_j}\frac{\Psi_j^{(k;j)}}{|\Psi_j^{(k;j)}|}\right)$

// OS/PIE updating for the probe position...
$\rho^{(k;j+1)} \longleftarrow \rho^{(k;j)} - \frac{\beta}{\max(|P|^2)}\partial_j$

end

// The real-space support constraint Π applied to the k-th update...
$\rho^{(k+1)} \longleftarrow \Pi\rho^{(k;J)}$

end

Noise amplification during 3DBPP phasing

In a transmission geometry, the numerical inversion of the x-ray projection operator $\mathcal{R}$ from experimental data, as implemented in computed tomography for example, is highly sensitive to noise [12, Sec. 4]. This sensitivity is a consequence of the Slice Projection Theorem. In the transmission geometry, the Fourier domain is "sliced" in polar coordinates, and high frequency components are sampled more sparsely as compared to low frequency components when the sample is rotated to measure the 3D intensity distribution. At a Bragg peak, on the other hand, the 3D intensity distribution can be measured with nearly parallel 2D slices as the sample is rocked in fine angular increments through the crystal rocking curve. This sampling of 3D reciprocal space at a Bragg peak is therefore done in a cartesian (though not orthogonal) frame [13] rather than a polar coordinate system. As a result, the high and low frequency components of a 3D Bragg peak intensity distribution are sampled equally, and this leads to a robust ptychographic reconstruction when angular diversity is utilized in the Bragg geometry to measure the 3D intensity distribution at each probe position.

For the 3DBPP technique introduced in this work, however, it is not clear *a priori* if the method will be sensitive to noise because the 3D sample information is extracted via shifting overlapping probe positions rather than polar or cartesian sampling of a 3D Fourier space far-field intensity distribution. Here, we addressed this issue by way of a numerical simulation. Coherent diffraction data was simulated from a 3D numerical test object (Figure S11) similar to the one featured in Figure 2 in the main text. While the ptychographic data was simulated in the same way as before, in this test the resulting intensity patterns were corrupted with Poisson noise in order to study its effects. From a starting guess of real random numbers, 100 iterations of OS/PIE were done in order to generate a starting estimate of the sample for the purposes of this test. From this starting estimate, 400 more iterations of the OS/PIE algorithm were performed, and the same object estimate was used as a starting point for 400 conjugate-gradient (CG) iterations. The CG inversion has been demonstrated to be convergent [14, Sec. 5.2], and hence provides (in the asymptotic limit) a local minimizer of the cost-function $\mathcal{Q}$ given by Equation 3 in the main text. In both cases, the reciprocal space error metric $\mathcal{Q}$ was tracked as a function of iteration number as well as the real space object error metric $||\rho - \rho_{orig}||^2$.

As shown in Figures S5(a, b), both algorithms minimize $\mathcal{Q}$, however their behavior is very different when evaluating how closely the reconstruction resembles the original object at each iteration in terms of $||\rho - \rho_{orig}||^2$. At first, the CG algorithm improves the quality of the result more rapidly than the OS/PIE algorithm (Figure S11(b)), however, after 52 iterations the CG $||\rho - \rho_{orig}||^2$ begins to increase, while $\mathcal{Q}$ continues to decrease. By contrast, with OS/PIE, the values of $||\rho - \rho_{orig}||^2$ and $\mathcal{Q}$ both decrease over the course of the 400 iterations (however, this is not necessarily an indication of convergence). According

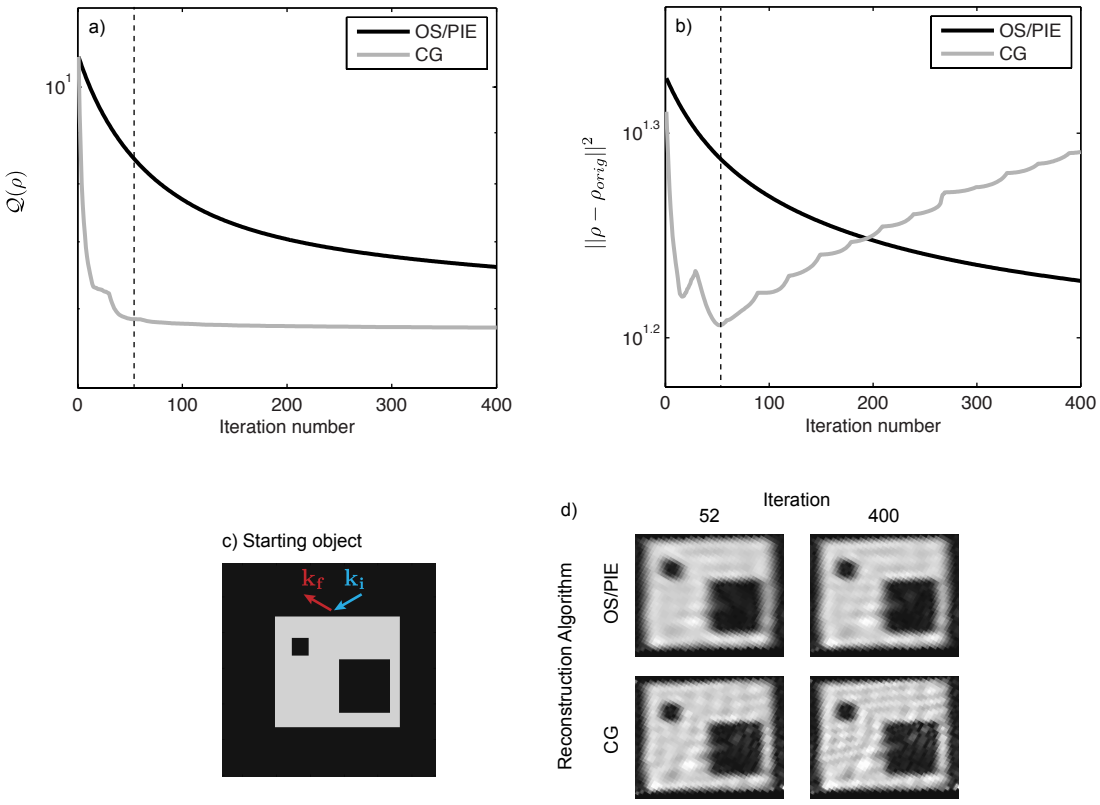

FIG. 11. Suppl. (S11). **3DBPP in the presence of noise.** (a) Evolution of the cost function $\mathcal{Q}$ and of the error metric in the object space $||\rho - \rho_{orig}||^2$ (b) shown as a function of iteration number for both the CG and the OS/PIE. (c) The cross-section through the center of the starting object ρ_{orig} and scattering geometry are shown. (d) Cross sections of the reconstruction ρ are shown at different iterations for the CG and OS/PIE strategies.

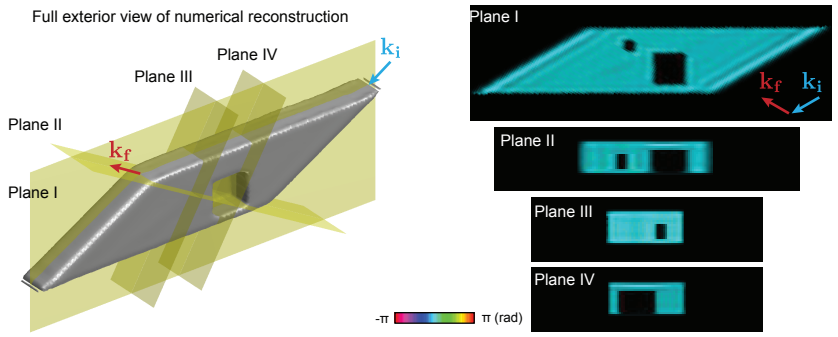

FIG. 12. Suppl. (S12). **3DBPP reconstruction demonstration.** A 50% isosurface of the full reconstructed volume of the numerical object in Figure 2 of the main text is shown on the left, together with four cut planes through the object. The reconstructed density along these cut planes (I-IV) is shown in the images on the right side. The smaller of the two voids in this object is completely enclosed within the surface rendering on the left, but can be seen in the cut planes. The cuts shown display reconstructed amplitude as brightness and phase as color (according to color scale shown).

to standard inversion theory [15, Sec. 6], the behavior displayed by the CG algorithm suggests that 3DBPP is noise sensitive, meaning that high-resolution features in the object cannot be retrieved from the noisy data set without regularization. However, stable band-limited reconstructions are obtained in the early iterations by the CG, and similar behavior can be obtained by other gradient-based iterative algorithms, including the OS/PIE as shown here. Despite the fact that the OS/PIE approach cannot reach (but will approach) the minimum of $\mathcal{Q}$ using noisy data because of the inherent properties of the algorithm, an OS/PIE-based reconstruction strategy was adopted in the work presented in this paper because it provides band-limited reconstructions [16, 17].

[1] Kak, A. C. and Slaney, M. *Principles of Computerized Tomographic Imaging*, IEEE Press (1988).

[2] Hruszkewycz, S. O., Holt, M. V., Allain, M., Chamard, V., Polvino, S., Murray, C. E., and Fuoss, P. H., Efficient modeling of Bragg coherent x-ray nanobeam diffraction. *Optics Letters*, **40,** 3241 (2015).

[3] Tomography with coherent x-rays has also been demonstrated with far field coherent x-ray Fourier synthesis methods that do not rely on backprojections. Rather, a 3D diffraction patterned assembled from individual 2D slices is phased and inverted [18, 19]. Also, in the transmission geometry, the curvature of the Ewald sphere has been used to extract 3D sample information [20]. In optics, a multi-slice approach has been introduced based on the breakdown of the projection approximation replaced by a multiple-scattering modeling, allowing to retrieve the exit-field along a series of finite-thickness slices [21].

[4] In this section, we assume the Fourier transform of a n-dimensionnal function ψ to be defined by $\tilde{\psi}(\boldsymbol{q}) = \int_{\mathbb{R}^n} \psi(\boldsymbol{r}) e^{-i\langle \boldsymbol{r},\boldsymbol{q}\rangle} \mathrm{d}\boldsymbol{r}$ with $i := \sqrt{-1}$. Conversely, the associated inverse Fourier transformation reads $\psi(\boldsymbol{r}) = \frac{1}{(2\pi)^n} \int_{\mathbb{R}^n} \tilde{\psi}(\boldsymbol{q}) e^{i\langle \boldsymbol{r},\boldsymbol{q}\rangle} \mathrm{d}\boldsymbol{q}$.

[5] Vartanyants, I. A., and Robinson, I. K., Partial coherence effects on the imaging of small crystals using coherent x-ray diffraction. *Journal of Physics – Condensed Matter*, **13,** 10593 (2001).

[6] Guizar-Sicairos, M., Holler, M., Diaz, A., Vila-Comamala, J., Bunk, O., and Menzel, A. Role of the illumination spatial-frequency spectrum for ptychography. *Physical Review B*, **86,** 100103(R) (2012).

[7] Dierolf, M., Menzel, A., Thibault, P., Schneider, P., Kewish, C. M., Wepf, R., Bunk, O. and Pfeiffer, F. Ptychographic X-ray computed tomography at the nanoscale. *Nature*, **467,** 436 (2010).

[8] Marchesini, S., He., H., Chapman, H. N., Hau-Riege, S. P., Noy, A., Howells, M. R., Weierstall, U., and Spence, J. C. H. X-ray image reconstruction from a diffraction pattern alone. *Physical Review B*, **68,** 140101(R) (2003).

[9] Harder, R., Liang, M., Sun, Y., Xia, Y., and Robinson, I. K.. Imaging of complex density in silver nanocubes by coherent x-ray diffraction. *New Journal of Physices*, **12,** 035019 (2010).

[10] van Heel, M., and Schatz, M. Fourier shell correlation threshold criteria. *Journal of Structural Biology*, **151,** 250 (2005).

[11] Vila-Comamala, J., Diaz, A., Guizar-Sicairos, M., Mantion, A., Kewish, C. M., Menzel, A., Bunk, O., and David, C. Characterization of high-resolution diffractive x-ray optics by ptychographic coherent diffraction imaging. *Optics Express*, **19,** 21333 (2011).

[12] Natterer, F. and Wübbeling, F. *Mathematical Methods in Image Reconstruction* (SIAM, Philadelphia, 2001).

[13] Berenguer, F., Godard, P., Allain, M., Belloir, J. M., Talneau, A., Ravy, S., and Chamard, V. X-ray lensless microscopy from undersampled diffraction intensities. *Physical Review B*, **88,** 144101 (2013).

[14] Nocedal, J. and Wright, S. J. *Numerical Optimization* (Springer, 2006).

[15] Bertero, M. and Boccacci, P. *Introduction to inverse problems in imaging* (IoP Publishing, Bristol, 1998).

[16] Godard P., Allain M., and Chamard V. Imaging of highly inhomogeneous strain field in nanocrystals using x-ray bragg ptychography: A numerical study. *Physical Review B*, **84,** 144109 (2011).

[17] Godard, P., Allain, M., Chamard, V., and Rodenburg, J. Noise models for low counting rate coherent diffraction imaging. *Optics Express*, **20 ,** 25915 (2012).

[18] Miao, J., Ishikawa, T., Johnson, B., Anderson, E., Barry, L. and Hodgson, K. O. High resolution 3D x-ray diffraction microscopy *Physical Review Letters*, **8,** 88303 (2002).

[19] Chapman, H. N., Barty, A., Marchesini, S., Noy, A., Hau-Riege, S. P., Cui, C., Howells, M. R., Rosen, R., He, H., Spence, J. C. H., Weierstall U., Beetz, T., Jacobsen, C., and Shapiro D. High-resolution *ab initio* three-dimensional x-ray diffraction microscopy *Journal of the Optical Society of America A*, **5,** 1179 (2006).

[20] Raines, K. S., Salha, S., Sandberg, R., Jiang, H., Rodriguez, J. A., Fahimian, B. P., Kepteyn, H. C., Du J., and Miao, J., Three-dimensional structure determination from a single view *Nature*, **463,** 214 (2010).

[21] Maiden, A. M., Humphry M. J., and Rodenburg J. M. Ptychographic transmission microscopy in three dimensions using a multi-slice approach *Journal of the Optical Society of America A*, **29,** 1606 (2012).